Scattering of evanescnet light by a finite-size probe in near-field scanning optical microscopy

doi: 10.1063/1.363519

Scattering of evanescent light by a finite-size probe in near-field scanning optical microscopy

Kenji Fukuzawa[a] and Hiroki Kuwano
NTT Interdisciplinary Research Laboratories, 3-9-11 Midori-cho, Musashino-shi, Tokyo 180, Japan

(Received 17 April 1996; accepted for publication 25 July 1996)

Scattering of the evanescent light by a finite-size SiO_2 probe is calculated using a point matching method in order to improve the efficiency collecting the near-field optical signal. The scattered-light patterns can be classified into three categories. Category 1 is where the probe tip radius is very small ($<\lambda/13$). Category 3 is where the probe radius is very large ($>\lambda/6$). Category 2 is the intermediate case ($\lambda/13<$radius$<\lambda/6$). When the radius is in category 1, the scattered light is able to be treated as a field radiated by the point dipole induced by the evanescent light at the probe tip. When the tip radius is in category 2 ($\lambda/13<$radius$<\lambda/6$), in order to obtain the angular distribution of the scattered light, the induced multipoles should be calculated, considering the probe radius and the incident angle. When the tip radius is in category 3 (radius $>\lambda/6$), the scattered light becomes larger in the parallel direction to a prism surface due to the forward scattering of the evanescent light.
 [S0021-8979(96)02221-9]

I. INTRODUCTION

The optical-characteristic distributions provided by near-field scanning optical microscopy (NSOM) have nanometer lateral resolution,[1–5] in contrast to the resolution of conventional optical microscopy, which is limited to about half the wavelength of the light source due to light diffraction. We previously proposed a semiconductor-based NSOM probe,[6,7] which we call a photocantilever. This microfabricated silicon cantilever has a *pn*-junction photodiode at its tip. This photodiode collects the propagating light that is converted from the evanescent light by the cantilever apex. By using this photocantilever-based NSOM, 20 nm gaps between small particles have been resolved.[8]

The conversion from evanescent light into propagating light is the key process in photocantilever-based NSOM as well as in photon scanning tunneling microscopy[9–11] (PSTM) and scanning tunneling optical microscopy[12] (STOM). We previously determined that the scattered light at the photocantilever apex is the main contributor to the NSOM signal.[13] In our analysis, the probe was assumed to be infinitely small, although the actual apex radius of the cantilever has finite size. Determining how a finite-size probe converts the evanescent field into scattered light is important for improving the efficiency collecting the scattered light for both scattered light-based NSOM[4,6,11] and PSTM.[9,10,12] It is also important to determine how small samples convert the evanescent field into scattered light.

In this article we investigate how a finite-size probe converts the evanescent field into scattered light by theoretically calculating the electromagnetic field and derive the guiding principles for NSOM probe design.

II. ELECTROMAGNETIC-FIELD CALCULATION

A. Point matching method

Models of the scattering of evanescent light have been based on both microscopic[14] and macroscopic approaches.[15] The microscopic approach is not suitable for a large probe because the model must be discretized which requires much time and memory for calculation. Barchiesi and van Labeke analytically determined the distribution of the scattered light;[15] however, they assumed that the probe is located far from the sample surface, although the distance between a probe and a sample is of the order of 1 nm in most NSOM experiments.

The point matching method (PMM), a commonly used method for calculating the electromagnetic field, has been used to calculate the distribution of the scattered light.[16] Novotny, Pohl, and Regli analyzed the electromagnetic field in aperture NSOM by using the multiple-multipole method, which is a PMM-extended method.[17] In PMM the distribution of the scattered light at any point can be calculated once the coefficients of the expansion functions have been determined so as to match the boundary values. This semianalytical numerical calculation method is suitable for calculating the scattering of a large probe, because only the surface of the probe must be discretized, not the probe volume.

B. Model geometry

In the model we use for a NSOM (Fig. 1), a spherical probe approaches the prism surface. The center of the probe is defined as the origin, and the vertical direction to the prism surface is defined as $\theta=\pi$. To reduce calculation time, a two-dimensional model is considered. After solutions symmetric and antisymmetric to the x axis are obtained, their sum is then calculated. The evanescent light is assumed to be generated at the prism surface. The incident light is an s-polarized plane wave. The model is divided into four regions. We focused on the scattered field distribution in region 3 because the scattered field in this region is detected as a NSOM signal.[4,6,11]

The electric field at point (r,θ) in the four regions is represented by the following series of expansions:

[a]Electronic mail:fukuzawa@ilab.ntt.jp

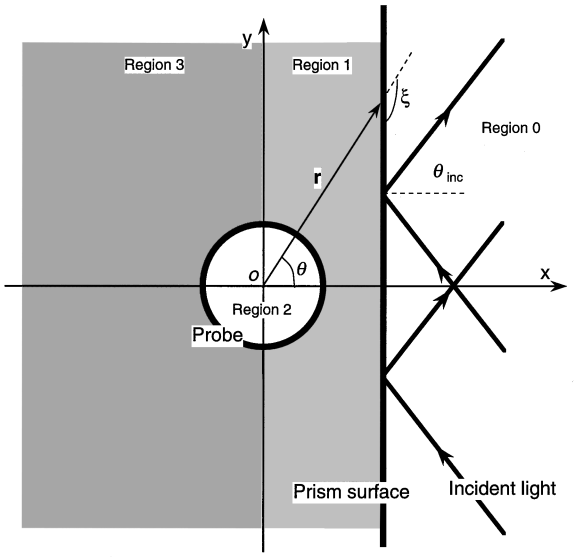

FIG. 1. Model for PMM analysis; refractive indices of the probe and prism are 1.44 and 1.51.

$$E_z^0(r,\theta)=\sum_{n=n_s}^{N_0+n_s} a_n^0 H_n(k_0 r) g(n\theta)+c_i E_z^{\mathrm{inc}}+c_r E_z^{\mathrm{ref}} \quad (\text{in region } 0), \tag{1}$$

$$E_z^1(r,\theta)=\sum_{n=n_s}^{N_1+n_s} [a_n^1 J_n(k_1 r)+b_n^1 Y_n(k_1 r)] g(n\theta)+c_e^1 E_z^{\mathrm{eva}} \quad (\text{in region } 1), \tag{2}$$

$$E_z^2(r,\theta)=\sum_{n=n_s}^{N_2+n_s} a_n^2 J_n(k_2 r) g(n\theta) \quad (\text{in region } 2), \tag{3}$$

$$E_z^3(r,\theta)=\sum_{n=n_s}^{N_3+n_s} a_n^3 H_n(k_3 r) g(n\theta)+c_e^3 E_z^{\mathrm{eva}} \quad (\text{in region } 3), \tag{4}$$

$$g(n,\theta)=\begin{cases}\cos(n\theta) & \text{for symmetric solution,}\\ \sin(n\theta) & \text{for antisymmetric solution,}\end{cases} \tag{5}$$

$$n_s=\begin{cases}0 & \text{for symmetric solution,}\\ 1 & \text{for antisymmetric solution,}\end{cases} \tag{6}$$

where J_n, Y_n, and H_n are a Bessel function of the first kind, a Bessel function of the second kind, and a Hankel function of the first kind, respectively. Additionally, k_i is the wave number in each region, and E_z^{inc}, E_z^{ref}, and E_z^{eva} are the incident, reflective, and transmitted evanescent lights, respectively, when the probe does not exist. In these solutions, the term $\exp(-i\omega t)$ is omitted. The sum of the Bessel functions of the first and second kind, which express the sum of the outgoing and incoming waves, is used in region 1 because multiple reflections between the probe and the prism occur in this region.

The boundary conditions are written as

$$E_z^i(r,\theta)=E_z^j(r,\theta) \quad (i,j=0,1,2,3), \tag{7}$$

$$\frac{1}{r}\frac{\partial E_z^i}{\partial\theta}\cos\xi+\frac{\partial E_z^i}{\partial r}\sin\xi = \frac{1}{r}\frac{\partial E_z^j}{\partial\theta}\cos\xi+\frac{\partial E_z^j}{\partial r}\sin\xi \quad (i,j=0,1,2,3), \tag{8}$$

where i and j are region numbers and ξ is the angle between the radial direction from the origin and the tangential direction of the boundary (Fig. 1). The coefficients of Eqs. (1)–(4) are determined so as to match the values at the boundary. Once these coefficient are determined, the electric field at an arbitrary point can be calculated using Eqs. (1)–(4).

III. RESULTS AND DISCUSSION

In this section we discuss the effect of probe size on the scattered-field distributions in region 3. Figure 2 shows the amplitude contours of the calculated electric fields around different-size probes. To clarify the scattered-field distribution, only the scattered fields are shown in the figure, that is, the electric fields of the incident, reflective, and transmitted plane wave are omitted. The wavelength of the incident light is 633 nm and the incident angle is 60°. The refractive indices in regions 0–3 are $n_0=1.51$, $n_1=1.0$, $n_2=1.44$, and $n_3=1.0$. The gap between the probe and prism is set at 1 nm. The incident light is an *s*-polarized plane wave. In this calculation, the electric-field vector is parallel to the *z* axis. When the probe radius is much smaller than the wavelength of the light, the scattered-field distribution is almost symmetric [$r=40$ nm, Fig. 2(a)]. The bigger the probe radius, the more asymmetric the angular distribution [$r=75$, 150 nm, Figs. 2(b) and 2(c)]. This tendency corresponds to an increase in the forward scattering component in the scattering of a propagating wave by a small particle.

Figure 3 shows the scattered-field angular distribution in the far field ($r=6.0$ μm) in region 3 for various probe sizes and incident angles. It shows the $|E|^2$ dependency on θ. The results suggest that we can define three categories. Category 1 is where the probe-tip radius is very small (less than about 50 nm, $\lambda/13$). Category 3 is where the radius is large (more than about 100 nm, $\lambda/6$). Category 2 is the intermediate case (from 50 to 100 nm, from $\lambda/13$ to $\lambda/6$).

In category 1 the field distribution is symmetric and there is little difference between the incident angles. The field intensity is almost uniform, from $\theta=3/4\pi$ to $5/4\pi$. If a single dipole is induced in the probe parallel to the incident electric field of the evanescent wave, the scattered field shows no difference in the angular distributions for different incident angles. It also shows a uniform distribution for θ because the incident wave is *s* polarized. Therefore, a single dipole parallel to the electric field of the evanescent wave is induced in category 1. Note that the intensity is larger around $\theta=\pi/2$ and $3/2\pi$ than around $\theta=\pi$. This is different from usual the Rayleigh scattering, and suggests that the influence of the substrate prism should be considered in evanescent-

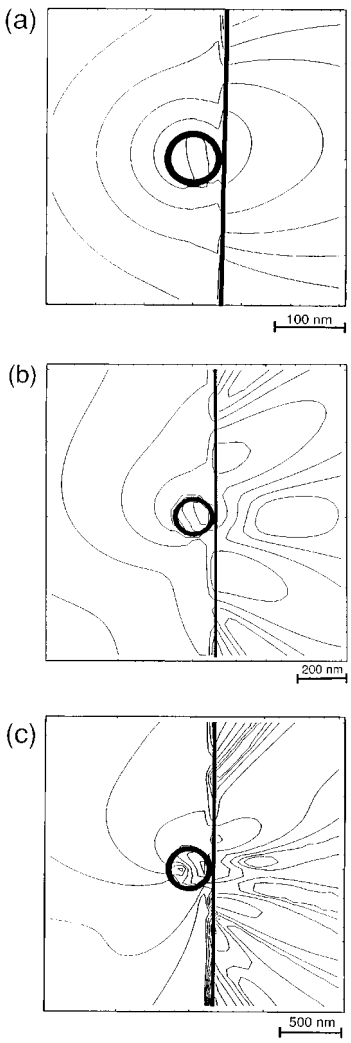

FIG. 2. Electric fields for various probe sizes. The incident angle is 60°, and scattered fields $|E|^2$ of the total field are shown in log scale. (a) $r=40$, (b) $r=75$, and (c) $r=150$ nm.

wave scattering. When a dipole is induced in the probe by the evanescent field, an image dipole is also induced. The positions of the probe and image dipole are symmetric to the prism surface, and the magnitude of the image dipole is larger by r_p than the probe dipole, where $r_p=-(\epsilon_s-1)/(\epsilon_s+1)$ and ϵ_s is the dielectric constant of the prism.[18] That is, two dipoles with opposite directions exist across the prism surface, and the gap between them is of probe radius order. This probe and image dipole act as a quadrapole; therefore, the scattered field has a strong intensity along the prism surface. In this calculation the interaction between the probe and prism surface is considered, so the difference between the scattering of the propagating and evanescent waves can be clarified. The scattered field from the collection angle of $\theta=3/4\pi$ to $5/4\pi$ mainly contributes to the near-field optical signal in the scattered-field-based NSOM. Therefore, for angular distributions, a probe with the radius of less than about 50 nm, $\lambda/13$, can be treated as a Rayleigh particle, which is so small that its size can be neglected.

In category 2 (from $r=50$ to 100 nm, from $\lambda/13$ to $\lambda/6$), the scattering pattern is more complicated. The angular distributions change from symmetric to asymmetric and have quite different patterns for different incident angles. This suggests that multipoles are induced and their generation is affected by the interaction between the probe and the prism. If a probe radius in this category is used, different collection efficiencies are expected for different incident angles, even if the collection angle of the detector is fixed. For a probe of the size in this category, the interaction between the probe and the sample should be considered.

In category 3 ($r>100$ nm, $\lambda/6$), the scattered field is largest in the direction of $\theta=\pi/2$. In addition, compared to region 2, the scattering patterns have smaller differences for the different incident angles. This suggests that forward scattering is the main contributor to the scattering wave in this region. The evanescent wave has a propagating component in the direction of $\theta=\pi/2$, and the light scattering has a large intensity in this direction due to the forward scattering of this propagating component. This is also the case for different incident angles, so the scattering patterns are only slightly different for different incident angles.

We derived the following guiding principles for improving the efficiency of collecting the near-field optical signal from our PMM-calculation results. When the tip radius of the probe is in category 1 (radius $<\lambda/13$), a single-point dipole is induced by an evanescent field at the probe tip and the scattered light is able to be treated as a field radiated by the point dipole. We can calculate the near-field optical signal after integrating the Poynting vector over the actual detector plane, considering the angular dependence of the field radiated by the point dipole. We previously reported this method to calculate the near-field signal in Ref. 13. PMM-calculation results indicate that this method is applicable to a finite-size probe whose tip radius is from zero to $\lambda/13$, although the probe size is assumed to be infinitely small. In addition, the collection efficiency is almost independent of the incident angle when the incident light is *s* polarized. When the tip radius is in category 2 ($\lambda/13<$tip radius$<\lambda/6$), the calculation of the near-field optical signal is rather complicated. The induced multipoles are quite different for the different probe sizes and incident angles. This indicates that the collection efficiency is strongly dependent on the incident angle, even if an identical probe is used. Calculating the near-field optical signal by using a probe in category 2 cannot be done using the same procedure as for a probe in category 1. Instead, the induced multipoles must be calculated, considering the probe radius and the incident angle. When the tip radius is in category 3 (radius $>\lambda/6$), the scattered light intensity becomes larger in the direction of $\theta=\pi/2$ due to forward scattering of the evanescent wave. Therefore, the efficiency of collecting the near-field signal is able to be improved by arranging the detector so as to collect the scattered light in this direction. In addition, the collection efficiency is almost independent of the incident angle when the incident light is *s* polarized.

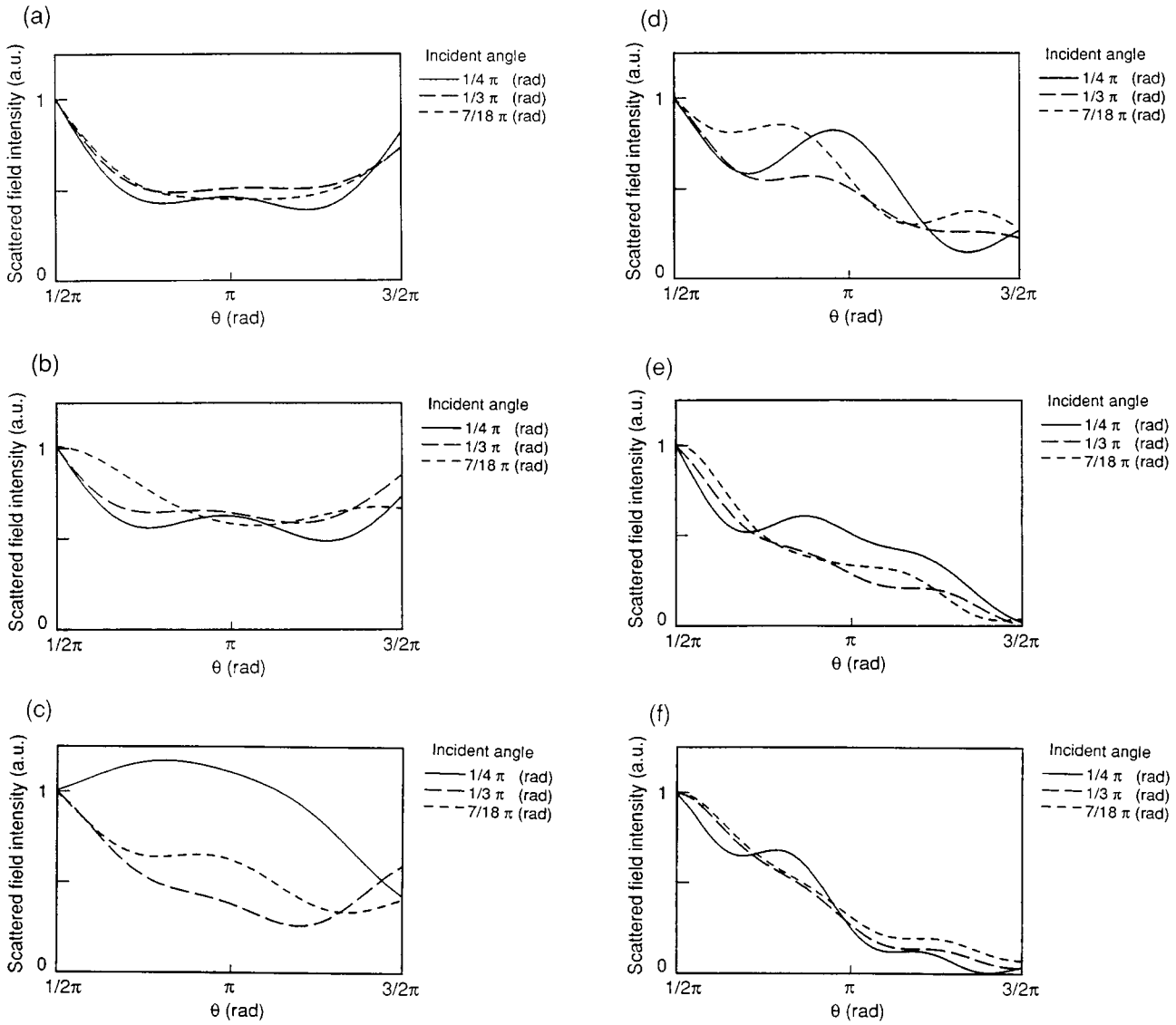

FIG. 3. Angular distributions of scattered field for different incident angles: $1/4\pi$, $1/3\pi$, and $7/18\pi$ (rad). (a) $r=40$, (b) $r=50$, (c) $r=75$, (d) $r=100$, (e) $r=125$, and (f) $r=150$ nm.

IV. CONCLUSION

We have determined the effect of probe size on the scattering pattern by using the point matching method. The patterns can be classified into three categories. Category 1 is for $r<\lambda/13$, category 3 is for $r>\lambda/6$, and category 2 is for the intermediate radii. When the tip radius of the probe is in category 1 (radius $<\lambda/13$), a single-point dipole is induced by the evanescent field at the probe tip, so the scattered light is able to be treated as a field radiated by the point dipole. When the tip radius is in category 2 ($\lambda/13<$radius$<\lambda/6$), in order to calculate the scattered-light distribution, the induced multipoles must be calculated, considering the probe radius and the incident angle. When the tip radius is in category 3 (radius $>\lambda/6$), the scattered light intensity becomes larger in the direction of $\theta=\pi/2$ due to the forward scattering of the evanescent wave.

ACKNOWLEDGMENTS

We are indebted to Naoto Kishi, Koichi Takiguchi, and Katsunari Okamoto for their suggestions on the PMM calculations. We thank Yuriko Tanaka for her comments on NSOM imaging.

[1] A. Lewis, M. Isaacson, A. Hrootunian, and A. Murray, Ultramicroscopy **13**, 227 (1984).
[2] D. W. Pohl, W. Denk, and M. Lanz, Appl. Phys. Lett. **44**, 651 (1984).
[3] E. Betzig and J. K. Trautman, Science **257**, 189 (1992).
[4] F. Zenhausern, M. P. O'Boyle, and H. K. Wickramasinghe, Appl. Phys. Lett. **65**, 1623 (1994).
[5] Y. Inouye and S. Kawata, Opt. Lett. **19**, 159 (1994).
[6] S. Akamine, H. Kuwano, K. Fukuzawa, and H. Yamada, in Proceedings of the IEEE workshop on Microelectromechanical Systems, 1995, p. 145.
[7] S. Akamine, H. Kuwano, and H. Yamada, Appl. Phys. Lett. **68**, 579 (1996).
[8] K. Fukuzawa, Y. Tanaka, S. Akanime, H. Kuwano, and H. Yamada, J. Appl. Phys. **78**, 7376 (1995).

[9] R. C. Reddick, R. J. Warmack, D. W. Chilcott, S. L. Sharp, and T. L. Ferrell, Phys. Rev. B **39**, 767 (1989).
[10] S. Jiang, H. Ohsawa, K. Yamada, T. Panagaribuan, M. Ohtsu, K. Imai, and A. Ikai, Jpn. J. Appl. Phys. **31**, 2282 (1992).
[11] N. F. van Hulst, M. H. P. Moers, O. F. J. Noordman, R. G. Tack, F. B. Segerink, and B. Bolger, Appl. Phys. Lett. **62**, 461 (1993).
[12] D. Courjon, K. Sarayeddine, and M. Spajer, Opt. Commun. **71**, 23 (1989).
[13] K. Fukuzawa and H. Kuwano, J. Appl. Phys. **79**, 8174 (1996).
[14] C. Girard and D. Courjon, Phys. Rev. B **42**, 9340 (1990).
[15] D. Barchiesi and D. van Labeke, Mod. Opt. **40**, 1239 (1993).
[16] See, for examples, M. Kerker, *The Scattering of Light and Other Electromagnetic Radiation* (Academic, New York, 1970).
[17] L. Novotny, D. W. Pohl, and P. Regli, J. Opt. Soc. Am. A **11**, 1768 (1994).
[18] O. Keller, S. Bozhevolnyi, and M. Xiao, *Near Field Optics* (Kluwer, Dordrecht, 1993).